Nanoscale

Stretching of Immersed Polyelectrolyte Brushes in Shear Flow

Journal:	*Nanoscale*
Manuscript ID	NR-ART-08-2023-004187.R1
Article Type:	Paper
Date Submitted by the Author:	02-Nov-2023
Complete List of Authors:	Qiao, Yijun; Argonne National Laboratory, Center for Molecular Engineering/Materials Science Division; Tsinghua University State Key Laboratory of Tribology He, Qiming; Argonne National Laboratory, Center for Molecular Engineering/Materials Science Division; University of Chicago, Pritzker School of Molecular Engineering Huang, Hsin-Hsiang; Argonne National Laboratory, Center for Molecular Engineering/Materials Science Division Mastropietro, Dean ; Argonne National Laboratory, Center for Molecular Engineering/Materials Science Division; University of Chicago, Pritzker School of Molecular Engineering Jiang, Zhang; Argonne National Laboratory Advanced Photon Source Zhou, Hua; Argonne National Lab, Advanced Photon Source Liu, Yuhong; Tsinghua University, Department of Mechanical Engineering Tirrell, Matthew; The University of Chicago, Molecular Engineering; Argonne National Laboratory, Center for Molecular Engineering/Materials Science Division Chen, Wei; Argonne National Laboratory, Center for Molecular Engineering/Materials Science Division; University of Chicago, Pritzker School of Molecular Engineering

ARTICLE

Stretching of Immersed Polyelectrolyte Brushes in Shear Flow

Yijun Qiao,[a,b] Qiming He,[a,c] Hsin-Hsiang Huang,[a] Dean Mastropietro,[a] Zhang Jiang,[d] Hua Zhou,[d] Yuhong Liu,[b,*] Matthew V. Tirrell,[a,c*] Wei Chen[a,c*]

Received 00th January 20xx,
Accepted 00th January 20xx

DOI: 10.1039/x0xx00000x

The way that polymer brushes respond to shear flow has important implications in various applications, including antifouling, corrosion protection, and stimuli-responsive materials. However, there is still much to learn about the behaviours and mechanisms that govern these responses. To address this gap in knowledge, our study uses *in situ* X-ray reflectivity to investigate how poly(styrene sulfonate) (PSS) brushes stretch and change in different environments, such as isopropanol (a poor solvent), water (a good solvent), and aqueous solutions containing various cations (Cs^+, Ba^{2+}, La^{3+}, and Y^{3+}). We have designed a custom apparatus that exposes the PSS brushes to both tangential shear forces from the primary flow and upward drag forces from a secondary flow. Our experimental findings clearly show that shear forces have a significant impact on how the chains in PSS brushes are arranged. At low shear rates, the tangential shear force causes the chains to tilt, leading to brush contraction. In contrast, higher shear rates generate an upward shear force that stretches and expands the chains. By analysing electron density profiles obtained from X-ray reflectivity, we gain valuable insights into how the PSS brushes respond structurally, especially the role of the diffuse layer in this dynamic behaviour. Our results highlight the importance of the initial chain configuration, which is influenced by the solvent and cations present, in shaping how polymer brushes respond to shear flow. The strength of the salt bridge network also plays a crucial role in determining how easily the brushes can stretch, with stronger networks offering more resistance to stretching. Ultimately, our study aims to enhance our understanding of polymer physics at interfaces, with a particular focus on practical applications involving polymer brushes.

1. Introduction

The structure at the surface plays a crucial role in determining the complex properties of novel materials.[1–3] For instance, switchable friction[4–6] in graphene is caused by reversible manipulation of striped adsorbates using a scanning probe microscope, while the super low friction in polyelectrolyte brushes results from the hydration layer around the charged polymer segments[7]. The friction[8,9] or adsorption properties[10,11] of surfaces can change under flow shear conditions. Understanding the structural response to flow shear and molecular behavior[12] is becoming increasingly important in uncovering the mechanisms of surface materials[13] such as antifouling surfaces[14–18]. Polymer brushes are ideal for studying structural response, as they are highly responsive to stimuli[19–22] and sensitive to various external factors, including solvent, ion concentration, valency, chemical nature[23], pH[24], and shear flow[10,11]. Further exploring how polymer brush structures respond in dynamic conditions will advance both the field of surface science and the technological applications of polymers[25–31].

The structural response of polymer brushes to flow shear has been studied, but there is still a lack of a widely accepted theoretical understanding of the interplay between fluid mechanics and polymer structure. Previous experiments[32–34] have shown conflicting results, with some studies reporting an increase in brush thickness under shear, while others suggest it remains unchanged or decreases. For example, Klein et al.[33] observed an increase in the thickness of a zwitterion-terminated polystyrene brush, while Rabin and Alexander's theoretical analysis[35–39] indicated no change. Neutral polystyrene brushes have also shown conflicting results, with some experiments indicating a decrease in thickness under shear[40], while others show no effect[41–45]. Despite the various methods used in these studies, the structural response of polymer brushes to shear remains unclear. Further investigation is needed to understand the impact of solvents[25] and electrostatic interactions[46] on the shear response of polymer brushes.

[a] *Materials Science Division and Centre for Molecular Engineering, Argonne National Laboratory, Lemont, Illinois 60439, USA.*
[b] *State Key Laboratory of Tribology, Tsinghua University, Beijing 100084, China.*
[c] *Pritzker School of Molecular Engineering, University of Chicago, Chicago. IL, 60637, USA.*
[d] *X-ray Science Division, Advanced Photon Source, Argonne National Laboratory, Lemont, Illinois 60439, USA.*
* Corresponding authors

Electronic Supplementary Information (ESI) available: XRR results of dry PSS brushes; AFM topographies of PSS brushes in solvents including water, IPA, and four nitrate solutions (Cs^+, Ba^{2+}, La^{3+}, Y^{3+}) with a concentration of 10 mM; the mass density and calculated $\delta$of the pure constituents and solutions used in the effective density models; the fitting parameters and the standard deviation from MCMC calculation; and the pH values of the above-mentioned solutions. See DOI: 10.1039/x0xx00000x

Polystyrene sulfonate (PSS) is a versatile and multi-functional polymer material. It can be used as a medication for high blood potassium, as a coating for electrodes to enhance robustness and conductivity,[47,48] and as a water-softening agent to remove metal ions from hard water. PSS brushes, when grafted, can serve as a high-performing water-based lubricant[7] with a friction coefficient below 0.001 when immersed in 6 mM $NaNO_3$ solution. However, the negatively charged nature of PSS brushes can result in their collapse[23] and formation of salt bridges with high-valence cations, which reduces their lubricity. A better understanding of the structural response of PSS brushes in shear flow will further advance their potential as a valuable engineering material.

In this study, we investigated the structural response of negatively charged PSS brushes under shear flow in multiple solution environments. PSS brushes were grafted on silicon substrates and immersed in different solutions, including a poor solvent (isopropanol, hereafter IPA), a good solvent (water), and aqueous solutions of $CsNO_3$, $Ba(NO_3)_2$, $La(NO_3)_3$, and $Y(NO_3)_3$. The electron density profiles (EDPs) of the brushes were analyzed using *in situ* X-ray reflectivity. The results revealed variations in brush thickness, chain stretching, and ion distribution, providing a comprehensive understanding of how PSS brush structures respond to shear flow. Further exploration of these findings could lead to advancements in interface science and potential applications of polymer brushes.

2. Experimental section

2.1 Materials

We purchased sodium 4-vinylbenzenesulfonate (technical, ≥90%), (3-aminopropyl) triethoxysilane (APTES, 99%), α-bromoisobutyryl bromide (98%), triethylamine (≥99%), toluene (anhydrous, 99.8%), 2,2- bipyridyl (bpy, ≥99%), Cu(I)Br (99.999%), methanol (≥99.9%), isopropyl alcohol (IPA) (≥99%), cesium nitrate ($CsNO_3$, 99%), barium nitrate ($Ba(NO_3)_2$, ≥99%), lanthanum(III) nitrate hexahydrate ($La(NO_3)_3{\cdot}6H_2O$, 99.99%), and yttrium(III) nitrate hexahydrate ($Y(NO_3)_3{\cdot}6H_2O$, 99.99%) from Aldrich and used them without further purification. Single-side polished silicon wafers (100 oriented, 4 in. diameter, 0.5 mm thickness) were purchased from university wafer (Boston, Massachusetts). Deionized water was prepared from a Millipore Milli-Q system with a resistivity of 18.2 MΩ·cm.

2.2 Synthesis of PSS Brushes

We synthesized PSS brushes through a surface-initiated atom transfer radical polymerization process.[23,49] The silicon wafer was cut into a 10mm x 55mm rectangle and thoroughly cleaned using a piranha solution. A layer of APTES was then deposited onto the silicon wafer through vapor deposition and annealed at 110°C in air for an hour. In the next step, a radical polymerization initiator, *α*-bromoisobutyryl bromide (2.37 mL, 19.2 mmol), was grafted onto the APTES monolayer in a toluene (60 mL) solution containing triethylamine (2.70 mL, 19.4 mmol). This process of surface-initiated atom transfer radical polymerization of PSS was carried out in a mixture of methanol and water solution (100 mL), along with sodium 4-vinylbenzenesulfonate (10 g, 48.2 mmol), Cu(I)Br (70 mg, 0.48 mmol), and bpy (150 mg, 0.96 mmol), under an inert gas environment after undergoing three freeze-thaw cycles. The reaction was allowed to proceed for 3 hours at room temperature, before being terminated by exposing the solution to air. The substrates were then rinsed with water and dried using a stream of nitrogen gas. The chemical structure of PSS is depicted in Figure 1(a).

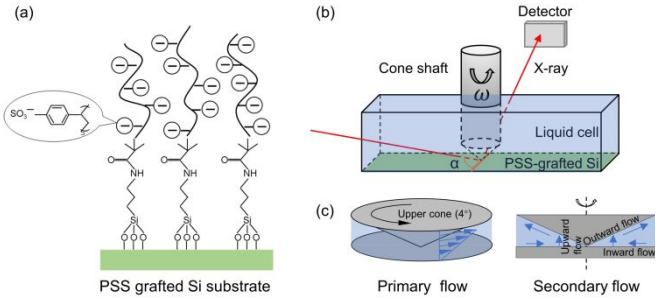

Figure 1. (a) Chemical structure depicting PSS brushes attached to a silicon substrate; (b) schematic illustrating the beam path during X-ray reflectivity measurement; and (c) diagram illustrating the primary and secondary flow within the cone-plate geometry.

2.3 *in situ* X-ray Reflectivity

X-ray reflectivity measurements were carried out at sector 12ID-D within the Advanced Photon Source, employing a custom-designed shearing setup featuring a cone-plate geometry.[32] This experimental setup entailed a beam of X-rays with an energy of 20.0 keV and dimensions of 500 μm x 76 μm (horizontal vs. vertical) traversing the liquid cell positioned at the center of the cone. By adjusting the rotational speed of the upper cone shaft, the shear rate—defined as the angular velocity of the upper cone divided by the cone angle—could be modulated. The cone itself, boasting an 8 mm diameter and a 4° angle, enabled the generation of both a purely tangential *primary* flow and a *secondary* flow engendered by centrifugal forces, inducing outward flow near the cone wall. This secondary flow was concurrent with an inward flow at the stationary wall and an upward flow in the gap, as exemplified in Figure 1(c).

Dry PSS brush samples were subjected to X-ray reflectivity assessment to evaluate film quality and ascertain brush thicknesses. Figure S1 demonstrated uniform reflectivity fringes for all dry brushes, indicative of a consistent brush structure and sound film quality. The brush thickness ranged between 14 and 20 nm. Subsequently, the dry PSS brushes were immersed in various solutions: IPA, water, and 10 mM solutions of $CsNO_3$, $Ba(NO_3)_2$, $La(NO_3)_3$, and $Y(NO_3)_3$. With shear flow rates spanning from 0 to 1,500 s^{-1}, X-ray reflectivity measurements were conducted following a stabilization period of 10 minutes.

The X-ray reflectivity data underwent analysis utilizing the effective density model[50,51] alongside the Hamiltonian Markov chain Monte Carlo (MCMC) method[52], facilitating the determination of the vertical Electron Density Profile (EDP) of the polymer brushes. The electron density, represented as $\rho_e = 2\pi\delta/(\lambda^2 r_e)$, is interconnected with the classical electron radius,

r_e = 2.8179403×10^{-15} m, the X-ray wavelength, λ, and the real part of the refractive index, $n = 1 - \delta + i\beta$, where δ and β denote the dispersive and absorptive attributes of X-ray matter interaction. Consequently, the δ-profile equates to the EDP with an offset of a constant value of $2\pi/(\lambda^2 r_e)$. Notably, while conventional reflectivity analysis typically incorporates a q_z-dependent damping term to account for roughness, this methodology is applicable solely to well-defined layered films with layer thicknesses significantly exceeding interface roughness. In cases where this criterion ($d \gg \sigma$) is unmet, the effective density model becomes indispensable, as it affords parameters suited for profile modeling rather than serving as definitive representations of physical layers. The effective density model, complemented by generalized skew-symmetric probability density functions,[51] was harnessed for the X-ray reflectivity data fitting of polymer brushes. Modeling the polymer brush necessitated one to three arbitrary layers, in addition to the thin SiO_x layer atop the silicon substrate. These interfacial layers—excluding the bottom-most (Si/SiO_x) and topmost (film/buffer) interfaces—were represented using the generalized skew-symmetric probability distribution function, preventing spurious penetration of the brush's δ-profile into the substrate during optimization. Parameters encompassing layer thickness, X-ray refractive index, roughness, and asymmetry factor for interfaces were pivotal in modeling these layers. The mass density and computed δ values for the pure constituents and solutions employed in the effective density models are detailed in Table S1 and S2 within the supporting information.

To undertake the Hamiltonian MCMC analysis, the No-U-Turn Sampler generated 5000 draws from the target posterior distribution for predictive modeling and confidence interval analysis. The 95% confidence intervals for reflectivity and EDP were calculated based on post-burn-in iterations. Hamiltonian MCMC as an efficient tool for the statistical analysis of the parameter distributions, as well as model predictions and confidence analysis.[52] Comprehensive details of fitting parameters and standard deviations ensuing from the MCMC calculations can be found in the supporting information (Tables S3-S8).

3. Results and discussion

3.1 Effect of Poor Solvent on Shear Response

Due to the limited solvation capability of PSS polymer brushes in isopropyl alcohol (IPA), the individual segments constituting the brush demonstrate a tendency to avoid direct interaction with solvent molecules. This phenomenon leads to a compacted chain conformation.[53] Our investigation focused on the structural behaviour of PSS brushes in IPA, subject to varying shear rates of 0, 30, 150, 300, and 750 s^{-1}.

The PSS brushes immersed in IPA exhibit two discernible regions: a densely packed layer and a diffuse layer, as inferred from the alterations in δ-profiles. As elucidated by the δ-profile presented in Figure 2(b) and corroborated by the layer thickness shown in Figure 2(c), the overall thickness of the PSS brushes in a quiescent IPA environment (0 s^{-1}) approximates 236 Å. This measurement slightly surpasses the thickness of the dry brush, indicative of a contracted structural configuration. Initially, the δ-profile of the PSS brush remains relatively constant in the vertical direction, followed by a gradual decline to the electron density corresponding to the IPA solvent. The transition point where this decline initiates and the δ-profile slope reaches -10^{-9}, a threshold designated on the δ-profiles of PSS brushes,

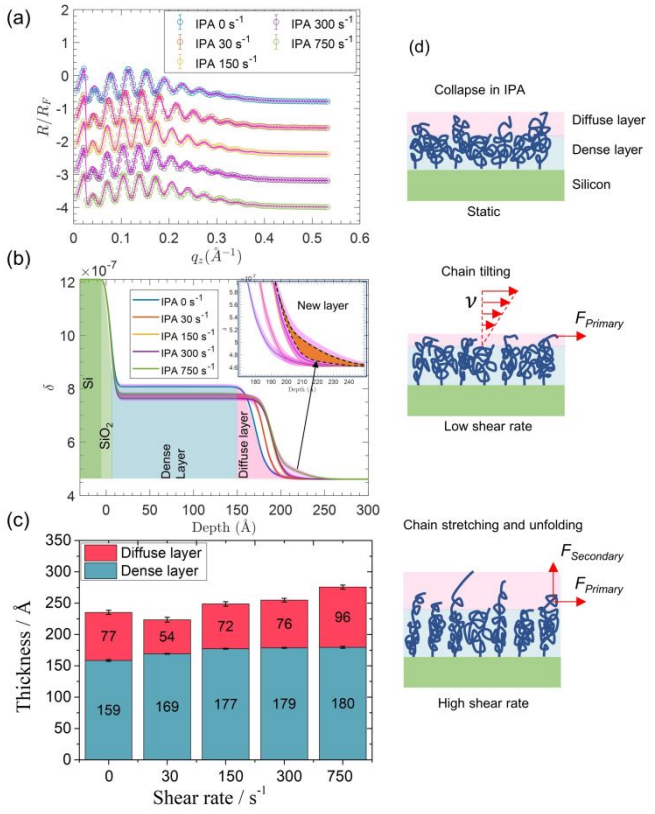

Figure 2. X-ray reflectivity analysis for PSS in IPA flow: (a) experimental reflectivity curves (coloured circles) with 95% confidence interval (magenta shaded area) derived from Hamiltonian MCMC analysis; (b) 95% confidence interval illustrating the δ-profile. The solid line denotes the median for PSS brushes subjected to shear rates of 0, 30, 150, 300, and 750 s^{-1} (inset depicting Si and SiO_2 layers of the substrate, along with dense and diffuse layers of brushes overlaid on the δ-profile); (c) fluctuations in thickness for dense and diffuse layers of PSS brushes under shear; and (d) schematic depiction of the structural transformations of PSS under IPA flow.

demarcates the boundary between the dense and diffuse layers. The selection of a critical slope value of -10^{-9} ensures the establishment of a uniform and stable electron density within the dense layer. This partitioning of the dense and diffuse layers aligns with conventional practice in polymer brush structural analysis.[54,55]

Conversely, the fluid's velocity within the flow only infiltrates a minor portion of the brushes and experiences a rapid diminishment within their interior.[56] The hydrodynamic penetration depth of the flow, commonly referred to as the slip length, is determined by extrapolating the linear region of the velocity profile in the far-field to the z-axis.[56] Consistent with Karniadakis's research[57] on polymer brushes subjected to shear flow, even under a substantial shear rate of approximately 10^{10} s^{-1}, the flow penetration remains restricted to the decay region of the density profile. Consequently, the unaffected internal

section of the polymer brush functions as a "solid wall."[56,57] Hence, our study follows the practice of demarcating the dense and diffuse layers based on the onset of δ-profile decay. This categorization ensures that the diffused layer is directly influenced by the shearing flow, while the dense layer remains less directly impacted.

The δ value within the dense layer of the PSS brush immersed in IPA registers approximately 8×10^{-7}, surpassing the δ value of pure IPA solvent. The δ contour of the PSS brush aligns with prior findings[58–60], revealing that PSS brush-solvent systems exhibit higher δ values compared to the pristine solvent.

When subjected to a low shear rate (30 s^{-1}), the PSS brushes in IPA exhibit an overall reduction in thickness. As depicted in Figure 2(c), the total brush thickness dwindles from 236 Å under static conditions to 223 Å at the low shear rate of 30 s^{-1}. Following this, the brush thickness demonstrates a tendency to increase and plateau across higher shear rates ranging from 30 to 300 s^{-1}. However, at the shear rate of 750 s^{-1}, there is a sharp increase in brush thickness, correlating with the emergence of a new layer as delineated in Figure 2(b).

The fluctuation in brush thickness finds its origin in the structural alterations occurring within the diffuse layer. Figure 2(c) reveals that while the thickness of the dense layer experiences a gradual increment across the shear rate range from 0 to 750 s^{-1}, the thickness of the diffuse layer follows a trend of initial reduction followed by augmentation with increasing shear rates. This behavior mirrors the overall brush thickness variation, thereby substantiating the supposition that the diffuse layer serves as the primary region for shear flow penetration.

The evolution of the polymer chain configuration can be deduced from the thickness variations. A schematic representation of the PSS brush chain configuration is provided in Figure 2(d). At low shear rates, where the secondary flow[61] remains negligibly weak, the dominant force is the tangential primary flow shear force, $F_{primary}$. This force prompts chain tilting along the direction of flow within the sparsely arranged diffuse layer, resulting in brush contraction. Concurrently, the dense layer experiences a slight stretching due to the pull exerted by polymer chains in the diffuse layer. With heightened shear rates, the upward shear force stemming from the secondary flow, $F_{secondary}$, collaborates with $F_{primary}$, causing both the diffuse and dense layers to undergo vertical chain stretching, thereby leading to brush expansion. The emergence of the new layer under the shear rate of 750 s^{-1} displays a distinctive δ-profile contour, signifying a distinct formation mechanism attributable to chain unfolding engendered by higher shear rates.

3.2 Effect of Good Solvent on Shear Response

Polymer brush structures primarily form due to the attractive interactions between the segments of the polymer brush and solvent molecules.[53] This attraction encourages the extension of the polymer chains into the solvent. In the case of negatively charged PSS brushes, the presence of charged monomers adds repulsive forces to the mix, contributing to the creation of a swollen structure characterized by stretched-out chains. These polymer chains move away from the surface to avoid

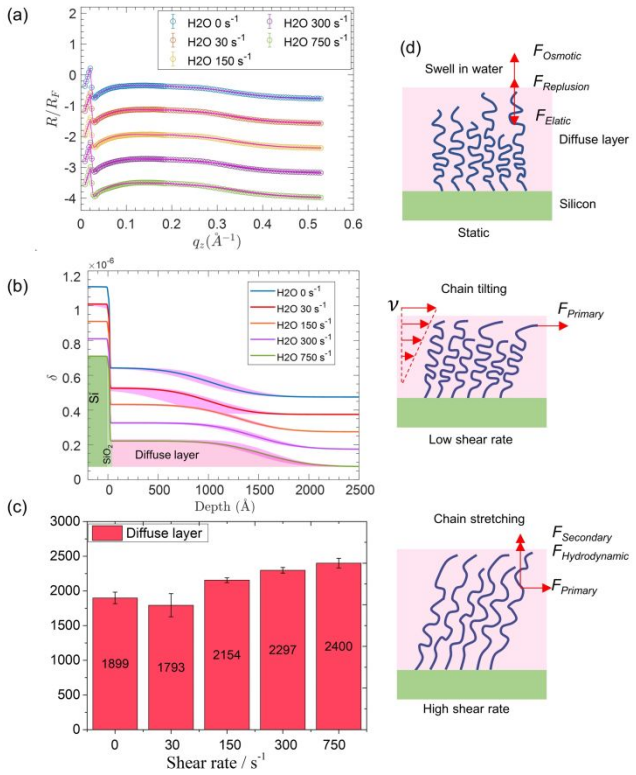

Figure 3. X-ray reflectivity analysis for PSS in salt-free water flow: (a) experimental reflectivity curves (coloured circles) with 95% confidence interval (magenta shaded area) obtained *via* Hamiltonian MCMC Analysis; (b) 95% confidence interval representing the δ-profile. The solid line represents the median for PSS brushes exposed to shear rates of 0, 30, 150, 300, and 750 s^{-1} (inset displaying Si and SiO_2 layers of the substrate, along with the diffuse layer of brushes superimposed on the δ-profile); (c) fluctuations in thickness for the diffuse layer of PSS brushes under shear; and (d) schematic depiction of the structural transformations of PSS under flow conditions in water.

unfavourable interactions between monomers. This stretching comes at the cost of their configurational entropy, often referred to as "stretching free energy." In this study, we examine how PSS brushes behave structurally when immersed in salt-free water under different shear rates, including 0, 30, 150, 300, and 750 s^{-1}.

When submerged in water, PSS brushes are treated as a single diffuse layer due to the presence of loosely arranged chains within the swelling structure. As depicted in Figure 3(c), the overall brush thickness under static water conditions measures approximately 1,899 Å, signifying a substantial swelling of PSS chains. Notably, the swollen PSS brushes in water exhibit a lower electron density compared to those in IPA, indicating a more relaxed chain distribution that can be penetrated deeply by the shearing flow.

Under the influence of a low shear rate (30 s^{-1}), the thickness of the PSS brushes experiences a decrease in water. This reduction is apparent from Figure 3(c), where the overall brush thickness diminishes from 1,899 Å under 0 s^{-1} to 1,793 Å under a shear rate of 30 s^{-1}. Subsequently, at higher shear rates ranging from 30 to 750 s^{-1}, a rapid increase in brush thickness is observed.

The structural and thickness variations within the diffuse layer of PSS brushes in water exhibit parallels to those observed in IPA. Under low shear rates, the tangential shear force of the

primary flow prompts chain tilting,[39] culminating in brush contraction. Conversely, under elevated shear rates, the involvement of the upward shear force from the secondary flow induces chain stretching, resulting in brush swelling. However, a unique feature in water is the contribution of hydrodynamic effects to chain stretching, a contrast to the behaviour observed in IPA. This phenomenon stems from the no-slip boundary condition at solid surfaces, which disrupts fluid flow symmetry around a chain and gives rise to an upward lifting force, denoted as $F_{hydrodynamic}$. Importantly, this lifting force, $F_{hydrodynamic}$, displays a positive correlation with shear rates, as elucidated by previous work.[62] While hydrodynamic interactions are restricted to a short distance for polymer brushes in poor solvents,[34] brushes in favourable solvents such as PSS brushes in water experience the cooperative influence of $F_{hydrodynamic}$ and the upward shear force, $F_{secondary}$, leading to chain stretching and an increase in brush thickness. A depiction of the chain behaviour of PSS brushes in water flow is provided in Figure 3(d).

3.3 Effect of Cations on Shear Response

The addition of electrolytes to solvents serves to mitigate the electrostatic repulsive forces between charged segments of polyelectrolyte brushes, and in certain scenarios, can lead to brush collapse *via* the formation of salt bridge networks.[23] In this context, we conducted an investigation involving the immersion of PSS brushes in aqueous solutions containing 10 mM $CsNO_3$, $Ba(NO_3)_2$, $La(NO_3)_3$, and $Y(NO_3)_3$. The corresponding pH values of these solutions are presented in Table S9, while the static solution morphologies of PSS brushes are visualized in Figure S2.

The addition of monovalent ions, such as Cs^+, to the solution noticeably affects the behaviour of PSS brushes. This change primarily results from the interaction between the charged PSS chains and Cs^+ ions. Specifically, when we introduce a solution containing 10 mM $CsNO_3$, the behaviour of these brushes falls into the "osmotic regime".[63,64] In this regime, the height of the PSS brushes is determined by a delicate balance between the pressure exerted by ions and the inherent elasticity of the polymer chains. When shear forces are applied, this balance is disrupted, leading to changes in the structure of the brushes.

In a 10 mM $CsNO_3$ aqueous solution, PSS brushes exhibit a swelling behaviour similar to their response in pure water, forming a single diffuse layer configuration. This behaviour is evident from the δ-profiles shown in Figure 4(b) and (c), where the overall brush thickness remains approximately 2,321 Å

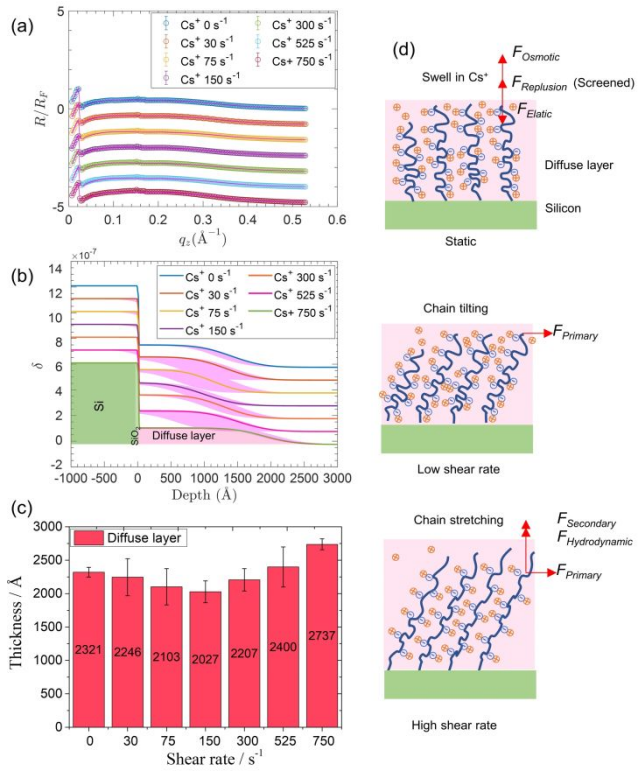

Figure 4. X-ray reflectivity analysis for PSS in 10 mM $CsNO_3$ aqueous solution: (a) experimental reflectivity curves (coloured circles) with 95% confidence interval (magenta shaded area) obtained through Hamiltonian MCMC analysis; (b) 95% Confidence Interval Representing the δ-profile. The solid line depicts the median for PSS brushes subjected to shear rates of 0, 30, 75, 150, 300, 525, and 750 s^{-1} (inset illustrating Si and SiO_2 layers of the substrate, along with the diffuse layer of brushes overlaying the δ-profile); (c) fluctuations in thickness for the diffuse layer of PSS brushes under shear; and (d) schematic depiction of the structural changes in PSS under flow conditions in a 10 mM $CsNO_3$ aqueous solution.

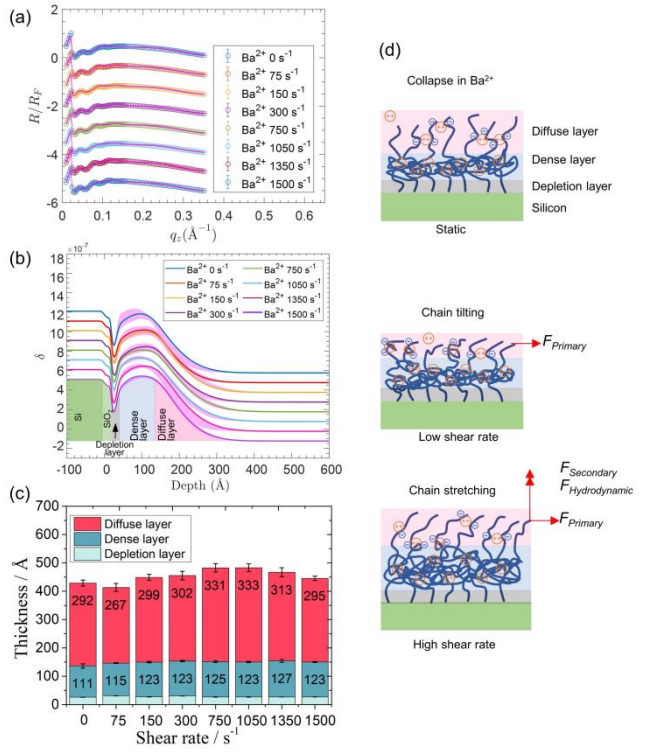

Figure 5. X-ray reflectivity analysis for PSS in 10 mM $Ba(NO_3)_2$ aqueous solution: (a) experimental reflectivity curves (coloured circles) along with a 95% confidence interval (magenta shaded region) attained through Hamiltonian MCMC Analysis; (b) 95% confidence interval representing the δ-profile. The solid line illustrates the median for PSS brushes subjected to shear rates of 0, 75, 150, 300, 750, 1,050, 1,350, and 1,500 s^{-1} (inset showing Si and SiO_2 layers of the substrate, along with the depletion layer, dense layer, and diffuse layer of brushes depicted along the δ-profile); (c) variations in thickness for the depletion layer (approximately 26 Å), dense layer, and diffuse layers of PSS brushes under shear; and (d) diagram depicting the structural alterations in PSS under flow conditions in a 10 mM $Ba(NO_3)_2$ aqueous solution.

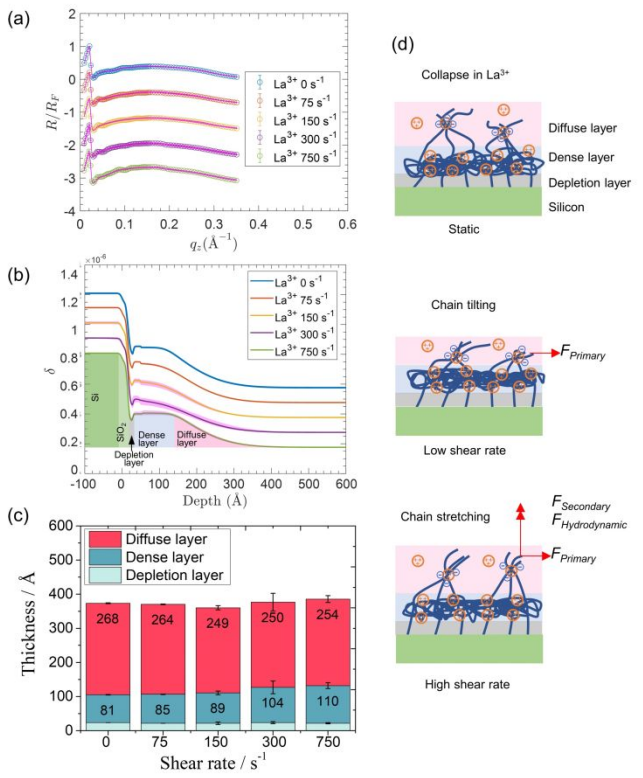

Figure 6. X-ray reflectivity analysis for PSS in 10 mM $La(NO_3)_3$ aqueous solution: (a) experimental reflectivity curves (coloured circles) with a 95% confidence interval (magenta shaded area) derived from Hamiltonian MCMC Analysis; (b) 95% confidence interval representing the δ-profile. The solid line indicates the median outcome for PSS brushes subjected to shear rates of 0, 75, 150, 300, and 750 s^{-1} (inset illustrating Si and SiO_2 layers of the substrate, along with the depletion layer, dense layer, and diffuse layer of brushes outlined along the δ-profile); (c) variations in thickness for the depletion layer (approximately 20 Å), dense layer, and diffuse layers of PSS brushes under shear; and (d) schematic representing the structural changes in PSS under flow conditions in a 10 mM $La(NO_3)_3$ aqueous solution.

under static conditions, indicating significant swelling. Interestingly, PSS brushes immersed in a Cs^+ solution show a notably greater thickness and lower electron density compared to those in IPA, indicating a loosely distributed chain arrangement and confirming their classification as a single diffuse layer.

When exposed to varying shear rates, the thickness of the diffuse layer consistently decreases from 0 to 150 s^{-1}, followed by an opposite trend of increase from 150 to 750 s^{-1}. Importantly, the presence of Cs^+ leads to a significant increase in the critical shear rate required for thickness augmentation, now reaching 150 s^{-1}. This contrasts with the behaviour in water, where the critical shear rate for thickness increase is 30 s^{-1}.

Regarding the hydrodynamic interactions, it is essential to note that these interactions become more pronounced with increasing shear rate. As the shear rate increases, the osmotic pressure exerted by counterions decreases, and the inherent elasticity of the polymer chains leads to the shrinkage of PSS brushes. This phenomenon may explain why the decrease in brush thickness occurs at higher shear rates, where significantly higher secondary flow is expected.

Upon immersion in $Ba(NO_3)_2$ solution, PSS brushes undergo collapse, leading to a structural division into three distinct sublayers: the depletion layer, dense layer, and diffuse layer. The cumulative brush thickness under static $Ba(NO_3)_2$ solution conditions measures 419 Å, notably smaller than the corresponding thickness in water, signifying a collapsed configuration. Notably, a region of low electron density near the substrate, termed the depletion layer, becomes evident. This depletion layer emerges from the non-uniform distribution of Ba^{2+} ions within the brush structure. Specifically, Ba^{2+} ions tend to adsorb by pairing with the sulfonic acid groups of PSS brushes, resulting in a rapid increase in electron density. These adsorbed ions impede the subsequent transformation and adsorption of subsequent ions, leading to a region with loosely distributed ions within the inner brush area adjacent to the substrate—termed the depletion layer. The brush section enriched with Ba^{2+} ions and marked by high electron density constitutes the dense layer, while the area in which the δ-profile decays to solution level encompasses the diffuse layer, serving as the primary region penetrated by shearing flow.

Under a low shear rate of 75 s^{-1}, the brush thickness experiences a reduction due to the influence of shear flow. This decrement is evident from Figure 5(c), where the overall brush thickness contracts from 419 Å under static conditions to 413 Å under

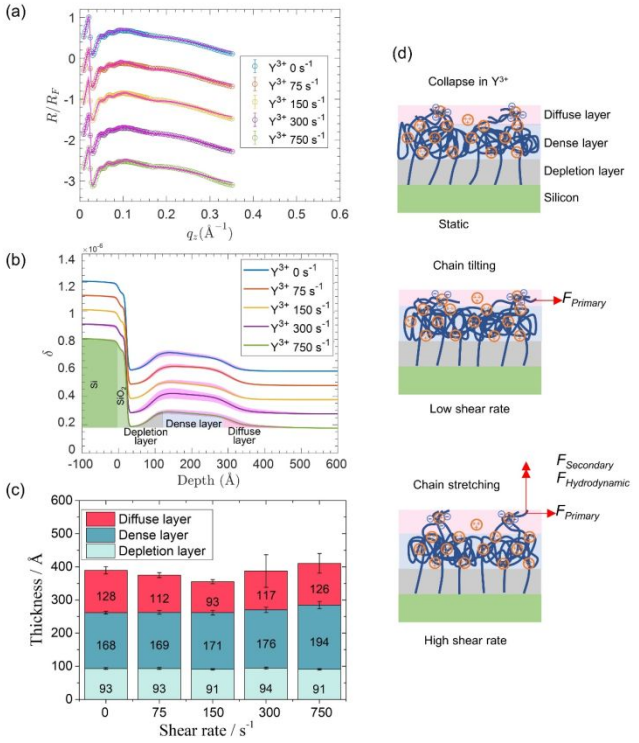

Figure 7. X-ray reflectivity analysis of PSS in 10 mM $Y(NO_3)_3$ aqueous solution: (a) experimental reflectivity curves (coloured circles) accompanied by a 95% confidence interval (magenta shaded area) obtained through Hamiltonian MCMC Analysis; (b) 95% confidence interval demonstrating the δ-profile. The solid line portrays the median outcome for PSS brushes exposed to shear rates of 0, 75, 150, 300, and 750 s^{-1} (inset illustrating Si and SiO_2 layers of the substrate, along with the depletion layer, dense layer, and diffuse layer of brushes depicted in relation to the δ-profile); (c) alterations in thickness for the depletion layer, dense layer, and diffuse layers of PSS brushes under shear; and (d) schematic depiction of the structural evolution of PSS under flow conditions in a 10 mM $Y(NO_3)_3$ aqueous solution.

shear conditions of 75 s^{-1}. Subsequently, with higher shear rates ranging from 75 to 750 s^{-1}, the brush thickness displays a consistent increase. However, beyond a shear rate of 1,050 s^{-1}, the brush thickness stabilizes and subsequently diminishes. The observed thickness variations in PSS brushes mirror their behaviour in IPA, attributed to the complicated structural fluctuations and rearrangements within the diffuse layer. Charged polyelectrolyte brushes tend to develop micelle-like structures[23,54] through the adsorption of salts and the establishment of salt bridge networks. These structures confer stability to the dense layer and render it less susceptible to the impact of flow shear. This behaviour is depicted in Figure 5(d), where polymer chains initially tilt along the tangential shear direction before subsequently undergoing vertical stretching.

In both trivalent La^{3+} and Y^{3+} nitrate solutions, PSS brushes experience collapse, as depicted in Figure 6(c) and Figure 7(c), leading to similar brush thicknesses of 373 and 389 Å, respectively. Notably, within the Y^{3+} solution, PSS brushes exhibit a broader depletion layer and dense layer, but a thinner diffuse layer compared to those immersed in the La^{3+} solution, indicating a more heterogeneous collapse phenomenon in the presence of La^{3+} ions.

PSS brushes within La^{3+} and Y^{3+} solutions exhibit parallel thickness variations under increasing shear rates. At low shear rates (0-150 s^{-1}), the brush thickness decreases due to a reduction in the thickness of the diffuse layer. Subsequently, at higher shear rates (150-750 s^{-1}), the brush thickness increases due to an expansion of the diffuse layer. However, PSS within the La^{3+} solution displays less thickness variation, reflecting a heightened resistance to deformation, likely attributed to the presence of a robust salt bridge network.

The interaction between cations and the $-SO_3^-$ groups within the PSS chain, along with cation radii, emerge as key determinants influencing the collapse structure and shear response of PSS brushes. Specifically, the solubility values of $La_2(SO_4)_3$ and $Y_2(SO_4)_3$, at 2.3 and 7.3 g/100mL respectively, provide a qualitative gauge of the coordination strength between cations and $-SO_3^-$ groups. Lower solubility values indicate a more potent coordination strength. Consequently, PSS brushes exhibit stronger interactions with La^{3+} ions, fostering the formation of robust salt bridges and facilitating a more heterogeneous chain collapse. Additionally, the cation radii of La^{3+} and Y^{3+} (1.22[39] and 0.93[40] Å respectively) influence their passage through interchain cavities, giving rise to a more uniform collapse structure with a thinner diffuse layer in the case of Y^{3+} ions.

3.4 Mechanism model of structural response to shear flow

The response of polymer brushes to shear flow, particularly the changes in thickness, has been a topic of debate in previous studies. Baker,[42,43] Nguyen,[41] others have explored neutral polystyrene brush copolymers using Neutron Reflectivity, with some concluding that flow shear does not impact brush thickness, while others reported varying thickness changes, including reduction at low shear rates and augmentation at high shear rates. Gutfreund and colleagues[40] conducted neutron reflectivity experiments and theoretical calculations, revealing polymer brush chain contraction under weak shear conditions below 30 s^{-1}. Charles and his team[65] introduced hydrodynamic and excluded volume interactions, predicting a thickness decline below 10 s^{-1}. Conversely, Harden[66,67] and others theorized that higher shear rates induced an increase in brush thickness. These varying observations underline the intricate nature of the interplay between shear forces, hydrodynamic interactions, and the initial configuration of polyelectrolyte brushes.

Our current study seeks to integrate these diverse theories and offer a comprehensive analysis of polymer brush thickness variation under shear. Figure 8(a) illustrates the normalized brush thickness of PSS in IPA, water, and four nitrate solutions under shear, revealing a discernible trend. PSS brush chains can be categorized into a depletion layer, dense layer, and diffuse layer based on δ-profile variations. The diffuse layer, notably

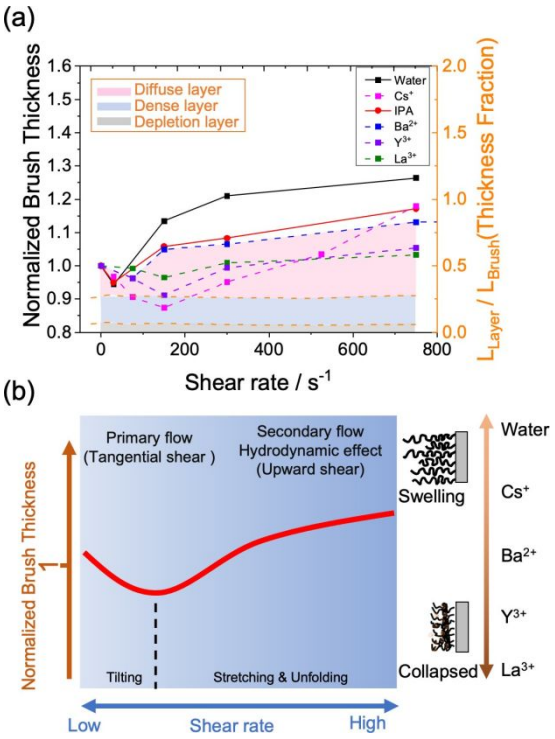

Figure 8. (a) normalized brush thickness variation with increasing shear rates for PSS brushes in IPA, water, and various cation (Cs^+, Ba^{2+}, La^{3+}, and Y^{3+}) solutions (thickness fractions of depletion layer and dense layer, and their shear-induced changes are illustrated using a coloured map); (b) schematic illustration depicting the structural response of PSS brushes in cation solutions under shear flow.

influenced by shear flow, plays a crucial role in the overall brush structural evolution. At low shear rates (0–150 s^{-1}), the brush thickness decreases initially due to polymer chain tilting, resulting in brush contraction. As shear rates increase (150–750 s^{-1}), the brush thickness rises due to polymer chain stretching, causing brush expansion.

Figure 8(b) provides a schematic illustration of the structural response of PSS brushes under shear. This response is influenced by the tangential shear force from primary flow, along with the upward shear force from secondary flow and hydrodynamic interaction. While the tangential shear force prevails at low shear rates, inducing chain tilting, the influence of secondary flow and hydrodynamic interaction becomes more pronounced with escalating shear rates.

The ability of the brush thickness to stretch vertically is intricately linked to the initial chain configuration within static solvents. As shown in Figure 8(a), the extent of stretching of PSS at 750 s^{-1} in different environments follows an order of water > Cs+ > IPA > Ba^{2+} > Y^{3+} > La^{3+}. The reduced stretching capacity of PSS in IPA compared to water indicates that the folding and entanglement of collapsed polymer chains increase resistance to deformation by shear flow. As depicted in Figure 8(b), PSS within multivalent cation solutions, displaying a collapsed structure, exhibits weaker stretching potential than PSS in water and monovalent Cs^{+} solutions. The decreased stretching ability of PSS brushes in trivalent $Y3^{+}$ and La^{3+} environments compared to IPA underscores the significance of the salt bridge network in determining resistance to stretching.

4. Conclusions

Our study focuses on understanding how PSS brushes respond structurally to shear forces by employing *in situ* X-ray reflectivity. We investigate this response in various solvent media, including water, IPA, and solutions containing different cation nitrates (Cs^{+}, Ba^{2+}, La^{3+}, Y^{3+}). The aim is to uncover the complex interactions between solvents and cations that influence the behavior of PSS brushes.

In water, PSS brushes adopt a swollen configuration, whereas they collapse when placed in IPA. The introduction of cations into the aqueous medium causes the PSS chains to collapse further, forming a robust salt bridge network. This network, characterized by its resistance to deformation, forms between the cations and the negatively charged polymer chains.

The interplay between shear forces and the initial chain structure plays a crucial role in governing the structural response of polymer brushes, particularly in terms of their thickness dynamics. At low shear rates, tangential shear forces cause the polymer chains to tilt along the shear direction, resulting in brush contraction. As shear rates increase, both secondary flow and hydrodynamic interaction generate an upward shear force, causing the polymer chains to stretch and leading to brush swelling.

The stretching capacity of polymer brushes is significantly influenced by both the collapsed structure and the presence of the salt bridge network. The order of stretching capacity for PSS in different solutions is as follows: water > Cs^{+} > IPA > Ba^{2+} > Y^{3+} > La^{3+}, highlighting the critical role of solution composition.

Our research, which investigates how polymer brushes respond in complex liquid environments under shear, provides valuable insights into the behavior of interfacial polymer chains. It sets the stage for further exploration, where additional factors such as chain length, counterions, and ion size will be carefully examined to enhance our understanding of polymer brush stretching behaviors. Ultimately, a more comprehensive theory in this area holds the potential to advance the practical applications of polymer brushes.

Conflicts of interest

There are no conflicts to declare.

Acknowledgements

Work in the Materials Science Division and Centre for Molecular Engineering of Argonne National Laboratory was supported by the U.S. Department of Energy, Office of Science, Office of Basic Energy Sciences, Materials Science and Engineering Division. Y. L. was supported by the Natural Science Foundation of China (No. 51875303). H.-H. H. acknowledges the financial support from 2019 New Partnership Program (108-2911-I-002-561). This research used resources of the Advanced Photon Source and the Centre for Nanoscale Materials, two U.S. Department of Energy (DOE) Office of Science User Facilities operated for the DOE Office of Science by Argonne National Laboratory under Contract No. DE-AC02-06CH11357. In addition, we gratefully acknowledge the computing resources provided on Bebop, a high-performance computing cluster operated by the Laboratory Computing Resource Centre at Argonne National Laboratory.

References

1 C. Feng and X. Huang, *Acc. Chem. Res.*, 2018, **51**, 2314–2323.
2 Y. Meng, J. Xu, Z. Jin, B. Prakash and Y. Hu, *Friction*, 2020, **8**, 221–300.
3 M. Li and C. W. Pester, *Polymers*, 2020, **12**, 1553.
4 P. Gallagher, M. Lee, F. Amet, P. Maksymovych, J. Wang, S. Wang, X. Lu, G. Zhang, K. Watanabe and T. Taniguchi, *Nat. Commun.*, 2016, **7**, 1–7.
5 W. Qian, T. Song, M. Ye, X. Huang, Y. Li and B. Hao, *J. Mater. Sci. Technol.*, 2022, **122**, 141–147.
6 W. Qian, T. Song, M. Ye, X. Huang, Y. Li and B. Hao, *J. Mater. Sci. Technol.*, 2023, **164**, 111–118.
7 J. Yu, N. E. Jackson, X. Xu, Y. Morgenstern, Y. Kaufman, M. Ruths, J. J. De Pablo and M. Tirrell, *Science*, 2018, **360**, 1434–1438.
8 Y. Gombert, R. Simič, F. Roncoroni, M. Dübner, T. Geue and N. D. Spencer, *Adv. Mater. Interfaces*, 2019, **6**, 1901320.
9 N. L. Cuccia, S. Pothineni, B. Wu, J. M. Harper and J. C. Burton, *Proc. Natl. Acad. Sci.*, 2020, **117**, 11247–11256.
10 B. Lopez-Mila, P. Alves, T. Riedel, B. Dittrich, F. Mergulhão and C. Rodriguez-Emmenegger, *Bioinspir. Biomim.*, 2018, **13**, 065001.
11 K. Yu, P. Andruschak, H. H. Yeh, D. Grecov and J. N. Kizhakkedathu, *Biomaterials*, 2018, **166**, 79–95.
12 S. Zhang, Y. Qiao, Y. Liu, L. Ma and J. Luo, *Friction*, 2019, **7**, 372–387.
13 Y. Li, Z. Jian, M. Lang, C. Zhang and X. Huang, *ACS Appl. Mater. Interfaces*, 2016, **8**, 17352–17359.
14 B. Xu, Y. Liu, X. Sun, J. Hu, P. Shi and X. Huang, *ACS Appl. Mater. Interfaces*, 2017, **9**, 16517–16523.
15 Y. Que, Y. Liu, W. Tan, C. Feng, P. Shi, Y. Li and H. Xiaoyu, *ACS Macro Lett.*, 2016, **5**, 168–173.
16 B. Xu, C. Feng, J. Hu, P. Shi, G. Gu, L. Wang and X. Huang, *ACS Appl. Mater. Interfaces*, 2016, **8**, 6685–6692.
17 B. Xu, G. Gu, C. Feng, X. Jiang, J. Hu, G. Lu, S. Zhang and X. Huang, *Polym. Chem.*, 2016, **7**, 613–624.
18 B. Xu, C. Feng, Y. Lv, S. Lin, G. Lu and X. Huang, *ACS Appl. Mater. Interfaces*, 2020, **12**, 1588–1596.
19 R. Wang, Q. Wei, W. Sheng, B. Yu, F. Zhou and B. Li, *Angew. Chem. Int. Ed.*, 2023, **62**, e202219312.
20 S. Ma, X. Zhang, B. Yu and F. Zhou, *NPG Asia Mater.*, 2019, **11**, 24.
21 S. Minko, *J. Macromol. Sci. Part C Polym. Rev.*, 2006, **46**, 397–420.

22 S. Peng and B. Bhushan, *RSC Adv.*, 2012, **2**, 8557–8578.
23 J. Yu, J. Mao, G. Yuan, S. Satija, Z. Jiang, W. Chen and M. Tirrell, *Macromolecules*, 2016, **49**, 5609–5617.
24 S. Ma, M. Scaraggi, P. Lin, B. Yu, D. Wang, D. Dini and F. Zhou, *J. Phys. Chem. C*, 2017, **121**, 8452–8463.
25 L. Wan, Y. Wang, X. Tan, Y. Sun, J. Luo and H. Zhang, *Friction*, , DOI:10.1007/s40544-020-0391-2.
26 J. Li, L. Gao, R. Xu, S. Ma, Z. Ma, Y. Liu, Y. Wu, L. Feng, M. Cai and F. Zhou, *Friction*, , DOI:10.1007/s40544-020-0389-9.
27 G. Zhang, G. Zheng, T. Ren, X. Zeng and E. van der Heide, *Friction*, 2020, **8**, 58–69.
28 J. Ma, C. Ma, X. Huang, P. H. H. de Araujo, A. K. Goyal, G. Lu and C. Feng, *Fundam. Res.*, 2023, **3**, 93–101.
29 W. Qian, T. Song, M. Ye, X. Huang, Y. Li and B. Hao, *Adv. Mater. Interfaces*, 2022, **9**, 2201611.
30 W. Qian, T. Song, M. Ye, X. Huang, Y. Li and B. Hao, *Compos. Commun.*, 2021, **23**, 100598.
31 Z. Wang, X. Jiang, W. Liu, G. Lu and X. Huang, *Sci. China Chem.*, 2019, **62**, 889–896.
32 Y. Qiao, H. Zhou, Z. Jiang, Q. He, S. Gan, H. Wang, S. Wen, J. de Pablo, Y. Liu, M. V. Tirrell and C. Wei, *Rev. Sci. Instrum.*, 2020, **91**, 013908.
33 J. Klein, D. Perahia and S. Warburg, *Nature*, 1991, **352**, 143–145.
34 V. Kumaran, *Macromolecules*, 1993, **26**, 2464–2469.
35 Y. Rabin and S. Alexander, *EPL Europhys. Lett.*, 1990, **13**, 49.
36 P.-Y. Lai and C.-Y. Lai, *Phys. Rev. E*, 1996, **54**, 6958.
37 P.-Y. Lai and K. Binder, *J. Chem. Phys.*, 1993, **98**, 2366–2375.
38 G. H. Peters and D. J. Tildesley, *Phys. Rev. E*, 1995, **52**, 1882.
39 L. Miao, H. Guo and M. J. Zuckermann, *Macromolecules*, 1996, **29**, 2289–2297.
40 A. Korolkovas, C. Rodriguez-Emmenegger, A. de los Santos Pereira, A. Chenneviere, F. Restagno, M. Wolff, F. A. Adlmann, A. J. Dennison and P. Gutfreund, *Macromolecules*, 2017, **50**, 1215–1224.
41 D. Nguyen, C. J. Clarke, A. Eisenberg, M. H. Rafailovich, J. Sokolov and G. S. Smith, *J. Appl. Crystallogr.*, 1997, **30**, 680–683.
42 S. M. Baker, A. Callahan, G. Smith, C. Toprakcioglu and A. Vradis, *Phys. B Condens. Matter*, 1997, **241**, 1041–1047.
43 S. M. Baker, G. S. Smith, D. L. Anastassopoulos, C. Toprakcioglu, A. A. Vradis and D. G. Bucknall, *Macromolecules*, 2000, **33**, 1120–1122.
44 R. Ivkov, P. D. Butler, S. K. Satija and L. J. Fetters, *Langmuir*, 2001, **17**, 2999–3005.
45 A. Korolkovas, P. Gutfreund, A. Chennevière, J. F. Ankner, F. A. Adlmann, M. Wolff and J.-L. Barrat, *Phys. Rev. E*, 2018, **98**, 032501.
46 H. Washizu, T. Kinjo and H. Yoshida, *Friction*, 2014, **2**, 73–81.
47 M. A. Zahed, S. C. Barman, P. S. Das, M. Sharifuzzaman, H. S. Yoon, S. H. Yoon and J. Y. Park, *Biosens. Bioelectron.*, 2020, **160**, 112220.
48 C. Duc, G. Stoclet, J. Soulestin and C. Samuel, *ACS Appl. Polym. Mater.*, 2020, **2**, 2366–2379.
49 B. Xu, C. Feng and X. Huang, *Nat. Commun.*, 2017, **8**, 1–8.
50 M. Tolan and M. Tolan, *X-ray scattering from soft-matter thin films: materials science and basic research*, Springer, 1999, vol. 148.
51 Z. Jiang and W. Chen, *J. Appl. Crystallogr.*, 2017, **50**, 1653–1663.
52 Z. Jiang, J. Wang, M. V. Tirrell, J. J. de Pablo and W. Chen, *J. Synchrotron Radiat.*, 2022, **29**, 721–731.
53 R. R. Bhat, M. R. Tomlinson, T. Wu and J. Genzer, *Surf.-Initiat. Polym. Ii*, 2006, 51–124.
54 D. Murakami, M. Kobayashi, Y. Higaki, H. Jinnai and A. Takahara, *Polymer*, 2016, **98**, 464–469.
55 I. E. Dunlop, R. K. Thomas, S. Titmus, V. Osborne, S. Edmondson, W. T. Huck and J. Klein, *Langmuir*, 2012, **28**, 3187–3193.
56 M. Deng, X. Li, H. Liang, B. Caswell and G. E. Karniadakis, *J. Fluid Mech.*
57 Y. Wang, Z. Li, J. Xu, C. Yang and G. E. Karniadakis, *Soft Matter*, 2019, **15**, 1747–1757.
58 P. Kaewsaiha, K. Matsumoto and H. Matsuoka, *Langmuir*, 2004, **20**, 6754–6761.
59 P. Kaewsaiha, K. Matsumoto and H. Matsuoka, *Langmuir*, 2007, **23**, 7065–7071.
60 H. Matsuoka, S. Nakayama and T. Yamada, *Chem. Lett.*, 2012, **41**, 1060–1062.
61 R. H. Ewoldt, M. T. Johnston and L. M. Caretta, in *Complex fluids in biological systems*, Springer, 2015, pp. 207–241.
62 C. E. Sing and A. Alexander-Katz, *EPL Europhys. Lett.*, 2011, **95**, 48001.
63 J. L. Harden and M. E. Cates, *Phys. Rev. E*, 1996, **53**, 3782–3787.
64 J. Yu, J. Mao, G. Yuan, S. Satija, Z. Jiang, W. Chen and M. Tirrell, *Macromolecules*, 2016, **49**, 5609–5617.
65 C. E. Sing and A. Alexander-Katz, *Macromolecules*, 2011, **44**, 9020–9028.
66 J. L. Harden, O. V. Borisov and M. E. Cates, *Macromolecules*, 1997, **30**, 1179–1187.
67 J. L. Harden and M. E. Cates, *Phys. Rev. E*, 1996, **53**, 3782.